The Magnetic Field in the Star-forming Region Cepheus A

from H$_2$O Maser Polarization Observations

W.H.T. Vlemmings[1], P.J. Diamond[1], H.J. van Langevelde[2,3], and J.M. Torrelles[4]

[1] Jodrell Bank Observatory, University of Manchester, Macclesfield, Cheshire, SK11 9DL, England
[2] Joint Institute for VLBI in Europe, Postbus 2, 7990 AA Dwingeloo, The Netherlands
[3] Sterrewacht Leiden, Postbus 9513, 2300 RA Leiden, The Netherlands
[4] Instituto de Ciencias del Espacio (CSIS)-IEEC, C/ Gran Capitá, 2-4, 08034 Barcelona, Spain; on sabbatical leave at the UK Astronomy Technology Centre, Royal Observatory Edinburgh, U.K.

13-10-2005

Abstract. We present linear and circular polarization observations of the H$_2$O masers in 4 distinct regions spread over 1×2 arcseconds around the HW2 high-mass young stellar object in the Cepheus A star-forming region. We find magnetic fields between 100–500 mG in the central maser region, which has been argued to trace a circumstellar disk. The masers further from HW2 have field strengths between 30–100 mG. In all cases the magnetic field pressure is found to be similar to the dynamic pressure, indicating that the magnetic field is capable of controlling the outflow dynamics around HW2. In addition to several H$_2$O maser complexes observed before, we also detect a new maser filament, $\simeq 1''$ ($\simeq 690$ AU) East of HW2, which we interpret as a shocked region between the HW2 outflow and the surrounding medium. We detect a linear polarization gradient along the filament as well as a reversal of the magnetic field direction. This is thought to mark the transition between the magnetic field associated with the outflow and that found in the surrounding molecular cloud. In addition to the magnetic field we determine several other physical properties of the maser region, including density and temperatures as well as the maser beaming angles.

Key words. star-formation – masers – polarization – magnetic fields

1. Introduction

While the process of low-mass star-formation has been well studied, high-mass star-formation is still poorly understood. Although several theories propose the formation of high-mass stars from the merger of several low-mass young stellar objects (e.g. Bonnell et al., 1998) recent studies and observations suggest that high-mass stars form, similar to low-mass stars, through accretion from a circumstellar disk (e.g. McKee & Tan, 2003; Patel et al., 2005; Jiang et al., 2005). In the prevailing picture of low-mass star-formation out of dense molecular clouds, strong magnetic fields support the clouds against a gravitational collapse. When self-gravity overcomes the magnetic pressure in the cloud core, the formation of protostars ensues (e.g. Shu et al., 1987; Mouschovias & Ciolek, 1999). Additionally, magnetic fields likely play an important role in many other stages of star-formation, such as the formation of bi-polar outflows and a circumstellar disk (e.g. Akeson & Carlstrom, 1997). Thus, accurate measurements of the magnetic field strength and structure in the densest areas of star-forming regions (SFRs) are needed to investigate the exact role of the magnetic field in both high- and low-mass starformation (see, e.g Sarma et al., 2001, 2002).

Through polarization observations, masers are excellent probes of magnetic field strength and structure in masing regions. For example, polarimetric SiO, H$_2$O and OH maser observations in the envelopes of evolved stars have revealed the strength and structure of the magnetic fields during the end-stages of stellar evolution (e.g Kemball & Diamond, 1997; Etoka & Diamond, 2004; Vlemmings et al., 2005) and H$_2$O maser polarization observations have provided stringent upper limits of the magnetic field in the megamaser galaxy NGC 4258 (Modjaz et al., 2005). SFRs also show a rich variety of maser species, including OH and H$_2$O . The OH masers are often found at several hundred to thousands AU from the SFR cores where the density n_{H_2} is less than a few times 10^8 cm^{-3}. Observations of the Zeeman effect on OH masers have been used to determine the SFR magnetic field in those regions (e.g Cohen et al., 1990; Bartkiewicz et al., 2005). The H$_2$O maser emission in SFRs is often associated with shocks created by the outflows of young stellar objects (YSOs) or with a circumstellar disk (Torrelles et al., 1996, hereafter T96; Gallimore et al., 2003, hereafter G03). The H$_2$O masers are excited in the dense parts of SFRs, with number densities n_{H_2} between approximately 10^8 and 10^{10} cm^{-3} (Elitzur et al., 1989). Because they are typically small (~ 1 AU), have a narrow velocity width (~ 1 km s^{-1}) and have a high brightness temperature $T_b > 10^9$ K

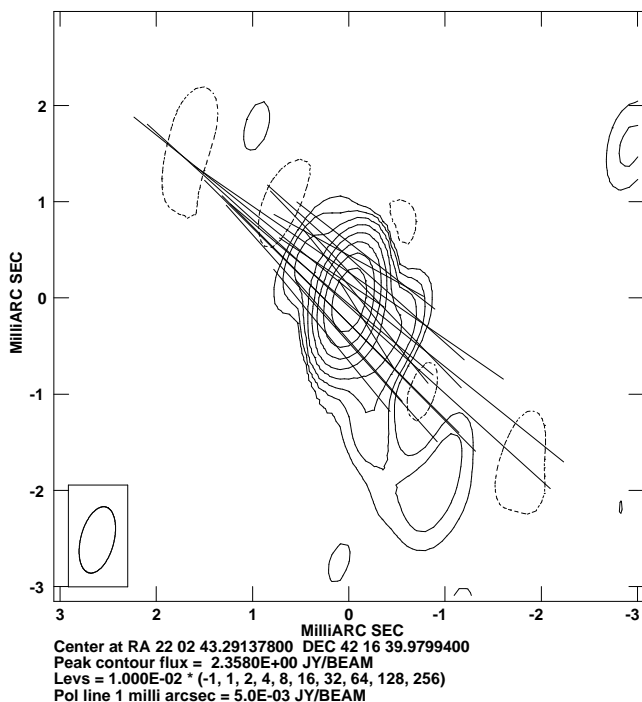*Send offprint requests to*: WV (wouter@jb.man.ac.uk)

Fig. 1. Total intensity (I) map with polarization vectors of our polarization calibrator J2202+4216 (BL Lac). The position angle (χ) of the vectors has been rotated by 77° so that it corresponds to the VLBA calibration observation.

(e.g. Reid & Moran, 1981), H_2O masers can be used to examine the small scale magnetic field strength and structure in dense parts of SFRs with polarimetric very long baseline interferometry (VLBI) observations. Previous VLBI observations have studied the linear polarization of H_2O masers as tracer of the magnetic field morphology in the SFRs W51 M (Leppänen et al., 1998), Orion KL and W3 IRS 5 (Imai et al., 2003). The circular polarization due to Zeeman splitting of the 22 GHz H_2O masers was first observed by Fiebig & Güsten (1989) with the Effelsberg 100m telescope. These observations were confirmed with VLBI by Sarma et al. (2001), who observed the H_2O maser circular polarization in W3 IRS 5 with the Very Long Baseline Array (VLBA). At lower spatial resolution, Sarma et al. (2002), also used the Very Large Array (VLA) to determine magnetic field strengths in a number of SFRs from H_2O maser observations. Here we present VLBA linear and circular polarization observations of the H_2O maser structures in the SFR Cepheus A HW2.

Cepheus A is a high-mass SFR located at a distance of ~725 pc (Johnson, 1957), which contains a large number of radio continuum sources (HW sources; Hughes & Wouterloot, 1984). Additionally it exhibits multi-polar outflows, NH_3 clouds, Herbig-Haro (HH) objects and infrared sources and a complex structure of OH, H_2O and methanol masers. The HW sources are compact HII regions that are thought to be excited by a YSO either externally or embedded in the HII cloud itself

(Cohen et al., 1984; Garay et al., 1996). The brightest of these sources is HW2 (Rodríguez et al., 1994), which is thought to contain the main exciting source in the SFR. Surrounding it is a rich structure of H_2O masers which has been studied in great detail (e.g T96; G03; Torrelles et al., 1998, 2001a,b, hereafter T98, T01a and T01b). More H_2O maser structures are found in clusters around other HW sources (HW3b and HW3d), $\simeq$ 4-5″ south from HW2 (T98; Lada et al., 1981; Cohen et al., 1984; Rowland & Cohen, 1986). The main, large scale, H_2O maser structure in the direction of HW2 was interpreted as tracing a 300 AU radius circumstellar disk perpendicular to the HW2 radio jet (T96). Recently, a flattened disk-like structure of dust and molecular gas with radius $\simeq$ 330 AU oriented perpendicular to and spatially coincident with the HW2 radio jet has been reported (Patel et al., 2005; Curiel et al., 2005).

Here we examine the polarization properties of the H_2O masers around Cepheus A HW2 and determine the magnetic field strength and structure. Additionally we describe the physical properties of the H_2O maser regions and discuss the detection of a new H_2O maser filament approximately 1″ East of the HW2 region.

The observations are described in § 2 and the results on the maser morphology and polarization are presented in § 3. The results are discussed in § 4, where intrinsic properties of the masing regions are derived. This is followed by a summary and conclusions in § 5 and § 6. The analysis method and the H_2O maser models used are presented in Appendix A.

2. Observations

The observations were performed with the NRAO[1] VLBA on October 3 2004. The average beam width is $\approx$ 0.5 × 0.5 mas at the frequency of the $6_{16} - 5_{23}$ rotational transition of H_2O, 22.235080 GHz. We used 4 baseband filters of 1 MHz width, which were overlapped to get a total velocity coverage of $\approx$ 44 km s^{-1}, covering most of the velocity range of the H_2O masers around the mean velocity of the H_2O masers of HW2 V_{lsr} = −11.7 km s^{-1} (T96). Similar to the observations in Vlemmings et al. (2002) (hereafter V02) of circumstellar H_2O maser polarization, the data were correlated multiple times with a correlator averaging time of 8 sec. The initial correlation was performed with modest spectral resolution (128 channels; 7.8 kHz= 0.1 km s^{-1}), which enabled us to generate all 4 polarization combinations (RR, LL, RL and LR). Two additional correlator runs were performed with high spectral resolution (512 channels; 1.95 kHz= 0.027 km s^{-1}), which therefore only contained the two polarization combinations RR and LL, to be able to detect the signature of the H_2O Zeeman splitting across the entire velocity range. The observations on Cepheus A HW2 were interspersed with 15 minute observations of the polarization calibrator J2202+4216 (BL Lac). Including scans on the phase calibrators (3C345 and 3C454.3) the total observation time was 8 hours.

2.1. Calibration

The data analysis path is described in detail in V02. It follows the method of Kemball et al. (1995) and was performed in the Astronomical Image Processing Software package (AIPS). The calibration steps were performed on the data-set with modest spectral resolution. Delay, phase and bandpass calibration were performed on 3C345, 3C454.3 and J2202+4216. Polarization calibration was performed on the polarization calibrator J2202+4216 (Fig.1). Fringe fitting and self-calibration were performed on a strong ($\sim$80 Jy beam^{-1}) maser feature (at $V_{lsr} = -15.72$ km s^{-1}). The calibration solutions were then copied and applied to the high spectral resolution dataset. Finally, corrections were made for instrumental feed polarization using a range of frequency channels on the maser source, in which the expected frequency averaged linear polarization is close to zero. In order to make a comparison with previous results we have used the AIPS task FRMAP in an attempt to determine the position of the reference feature before any self-calibration or fringe fitting. Though an exact position determination was impossible, we found it to be within $\sim$25 mas of our pointing position ($\alpha(J2000) = 22^h56^m17\overset{s}{.}977$ and $\delta(J2000) = +62°01'49''.419$), which was the brightest maser feature of the maser region R4 from G03.

An initial image cube with low resolution (2048$\times$2048 pixels of 1 mas) was created from the modest spectral resolution data set using the AIPS task IMAGR. In this cube a search was performed for maser features and 4 distinct regions with maser emission were detected (further labeled I through IV; shown in Fig. 2). For these fields, typically $\sim$100$\times$100 mas in size, IMAGR was used to create high spatial resolution (1024$\times$1024 pixels of 0.09 mas) Stokes I, Q and U image cubes from the modest spectral resolution data set. Stokes I and V cubes for the same regions were created from the high spectral resolution data set. In the high spectral resolution total intensity channel maps, the noise ranges from $\approx$15 mJy in the channels with weak maser features, to $\approx$35 mJy when dominated by dynamic range effects in the channels with the strongest maser features. In the circular polarization polarization maps the rms noise is $\approx$15 mJy. In the lower resolution Stokes Q and U maps the rms noise is $\approx$ 10 mJy.

Unfortunately, we found that in a small range of frequency channels where a higher frequency band overlaps the neighboring lower band, cross-talk between the sub-bands resulted in unreliable calibration. Although we were able to image the masers in those channels (V_{lsr} between -12.8 km s^{-1} and -13.5 km s^{-1} as well as between -1.2 km s^{-1} and -2.5 km s^{-1}) they were not included in our polarization analysis as the calibration accuracy was insufficient.

To calibrate the polarization angle $\chi = 1/2 \times atan(U/Q)$ of the resulting maps, the polarization calibrator J2202+4216 was mapped using the full 4 MHz bandwidth. The resulting map with polarization vectors is shown in Fig. 1. The polarization vectors were rotated to match the polarization angle of J2202+4216 determined in the VLBA polarization calibration observations [2]. As our observations were made exactly be-

tween two of the calibration observations on September 19 and October 17 2004 where the polarization angle of J2202+4216 changed from 41° to 57°, we use the average of 49°. Thus, we estimate our polarization angles to contain a possible systematic error of $\sim$8°.

2.2. Cepheus A HW2

We detected 4 distinct regions of H_2O maser emission between $V_{lsr} = -22.5$ and 0.5 km s^{-1}. We did not detect any of the maser features with positive velocity from T98 and T01a to a limit of $\approx$45 mJy. In Fig. 2 we show a 2.3$''$ × 2.3$''$ area around HW2 in which the fields where H_2O maser emission was detected are marked. We also indicate the continuum source HW2 (T96) and the location of previously detected H_2O maser not visible in our observations. Additionally, the location of OH masers (Bartkiewicz et al., 2005) and 12 GHz methanol masers (Minier et al., 2001) are plotted. All offset positions in this paper are given with respect to reference maser feature position at $V_{lsr} = -15.72$ km s^{-1} which was earlier found to be within 25 mas of our pointing center. The accuracy of each individual maser feature position can be estimated by Beamsize/SNR, which is typically better than $\sim$0.005 mas. In our polarization analysis we only considered maser features with intensities > 1 Jy.

3. Results

3.1. Distribution of the Maser Features

In Fig. 3 we show the 4 fields in which maser features stronger than 1 Jy beam^{-1} were identified. The hexagonal symbols denoting the maser features are scaled logarithmically by their flux density level. We identified 54 maser features although 14 of those had a velocity located in the ranges that suffered from interference as discussed above. The maser features are listed in Table 1 with their positional off-set from the reference maser position, peak flux density, radial velocity V_{lsr} and full width half maximum (FWHM) Δv_L. The positions were determined in the frequency channel containing the peak Stokes I emission using the AIPS task JMFIT. The masers in Field I, III and IV were seen previously (T01b) while Field II contains a newly detected linear maser structure approximate 1$''$ East of HW2 (assuming a distance of 725 pc the masers are located $\sim$690 AU from HW2). The masers in Field I are identified as the masers seen in the region labelled R4 of T01b observed with similar lsr velocity. This are also the masers that were hypothesized to belong to a rotating disk in G03 and are found over a large velocity range (V_{lsr} between -20 and 0 km s^{-1}). As seen in Fig. 2, the maser structure in Field II is located close to the brightest of the 12 GHz methanol maser features detected by Minier et al. (2001). However, the methanol masers at $V_{lsr} = -4.2$ km s^{-1} are significantly red-shifted with respect to the H_2O maser structure, which has an average $V_{lsr} \sim -13.7$ km s^{-1}. The 2 maser features in Field III at $V_{lsr} \approx -8.5$ km s^{-1}, correspond to a small part of the extended maser arc in R5 of T01b. This arc was identified to belong to a spherical shell around an embedded YSO (Curiel et al., 2002). The fairly weak masers of Field
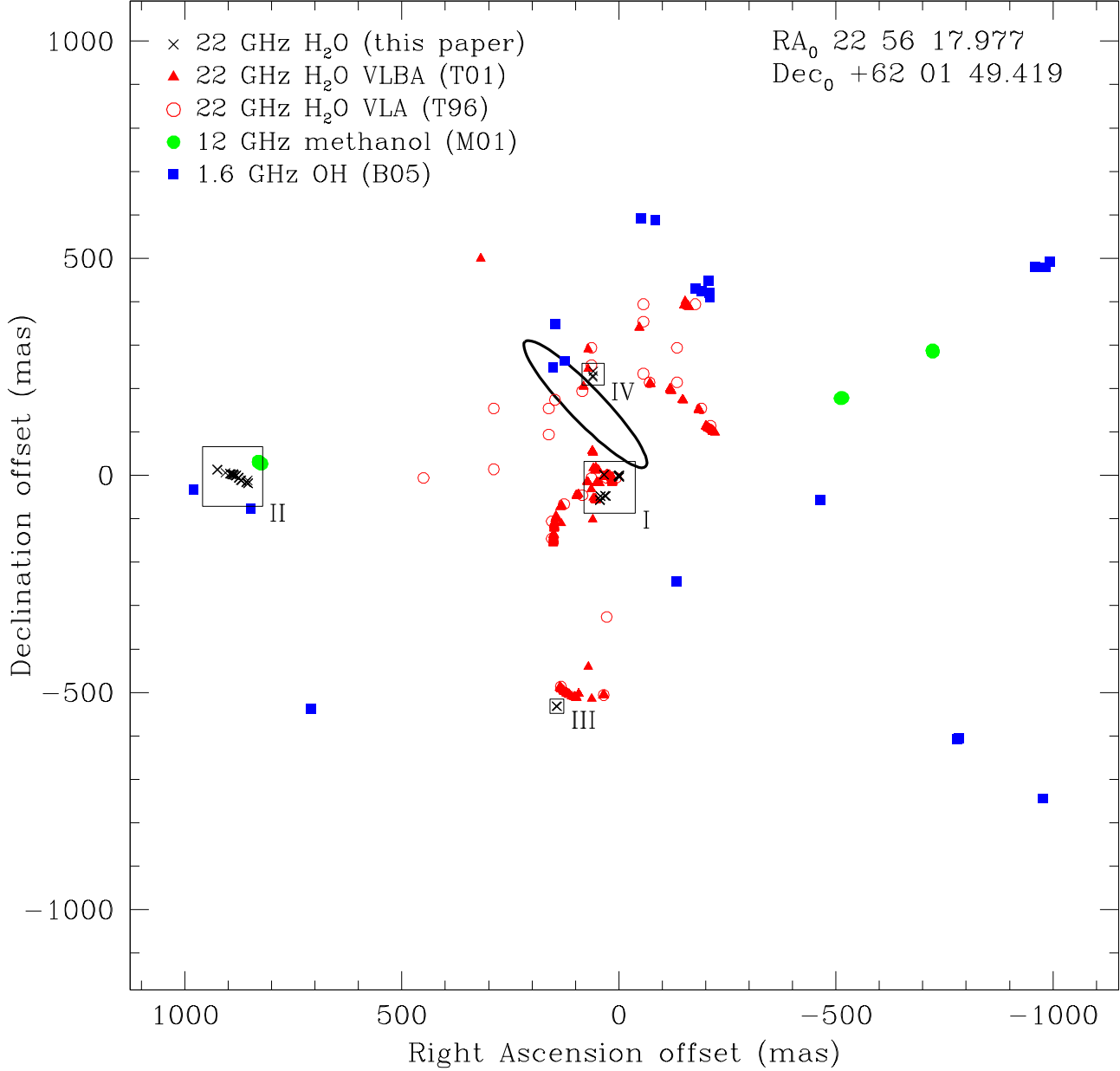
Fig. 2. The Cepheus A HW2 region with related maser features. The crosses indicate the H_2O maser features from our observations with the boxes labeled I through IV the fields in which the masers where detected. The other H_2O maser positions are from the VLA and VLBA observations in T96 and T01 respectively. The solid dots are the positions of the 12 GHz methanol masers from Minier et al. (2001) (M01) The solid squares are the 1665 and 1667 MHz OH masers observed by Bartkiewicz et al. (2005) (B05). The ellipse denotes the position and shape of the HW2 continuum emission at 1.3 cm (T96).

IV at $V_{lsr} \approx -21$ km s^{-1} are located closest to HW2 and likely correspond to a few isolated features detected in T96. We did not detect any of the masers from the arc-like structures in R1, R2 and R3 of T01b. The total extent of the region in which we detected maser emission is $\sim 950 \times 790$ mas, corresponding to 690×575 AU.

3.2. Circular Polarization

Circular polarization between 0.018–2.31% was detected in 14 of the 40 maser features that did not suffer from the frequency band overlap interference. Features that were not analyzed due to the interference are marked in Table 1. This table also shows the circular polarization fraction P_V as well as the magnetic

Fig. 3. A close-up view of the 4 fields in which we detected H_2O maser features. The octagonal symbols are the identified maser features scaled logarithmically according to their peak flux density. The maser velocity is indicated by color, note that the color scale is different for the 4 fields. A 10 Jy beam^{-1} symbol is plotted for illustration in the lower left corner of Field IV. The linear polarization vectors, scaled logarithmically according to polarization fraction P_l, are over-plotted. For the maser features where the Zeeman splitting was detected the magnetic field strength is indicated in mG.

field strengths along the line of sight with 1σ errors or 3σ upper limits determined by comparing the line width and circular polarization with models of non-LTE radiative transfer in the magnetized H_2O molecules (Appendix A). As the 1σ errors include both the formal fitting uncertainties as well as the contribution of the error in the model Δv_{th} (thermal line width) and $T_b\Delta\Omega$ (emerging maser brightness temperature in K sr), the magnetic field strength can occasionally be $< 3\sigma$, even though the circular polarization signal has a SNR higher than 3. The table also includes the best fit model values for Δv_{th} and $T_b\Delta\Omega$, where the emerging brightness temperature has been scaled with maser decay and cross-relaxation rate as described in Appendix A. The errors on these are estimated there to be 0.3 km s^{-1} in Δv_{th} and 0.4 on log($T_b\Delta\Omega$). As the lack of circular polarization introduces an additional free parameter in

the model fitting, significantly increasing the Δv_{th} and $T_b\Delta\Omega$ errors, we do not fit for maser features that do not show circular polarization. The magnetic field strength ranges from several tens of mG in Fields II and III to several hundred mG in Field I and is seen to switch direction on small scales in both Field I and II. Note that a positive magnetic field values indicates a field pointing away from the the observer. Total intensity (I) and circular polarization (V) spectra of several of the maser features are shown in Figs. 4 and 5. The spectra include the best fit model for the circular polarization.

3.3. Linear Polarization

In addition to the circular polarization, we detected linear polarization in approximately 50% of our maser features. The
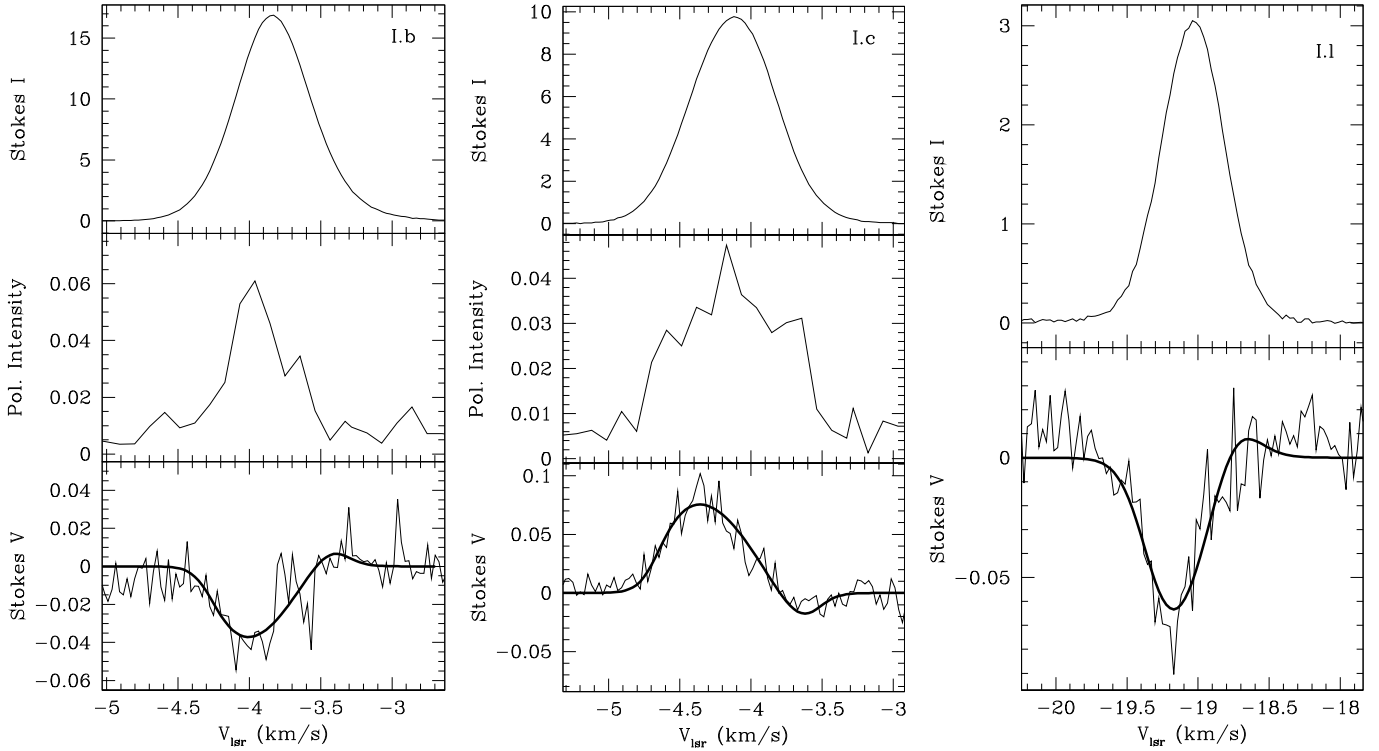
Fig. 4. Total power (I) and V-spectra for selected maser features of Field I. Additionally, the linear polarized flux density, $\sqrt{(Q^2 + U^2)}$, is shown when detected. The flux densities are given in Jy beam^{-1}. The thick solid line in the bottom panel shows the best non-LTE model fit to the circular polarization V. The V-spectrum is adjusted by removing a scaled down version of the total power spectrum as indicated in Appendix A.
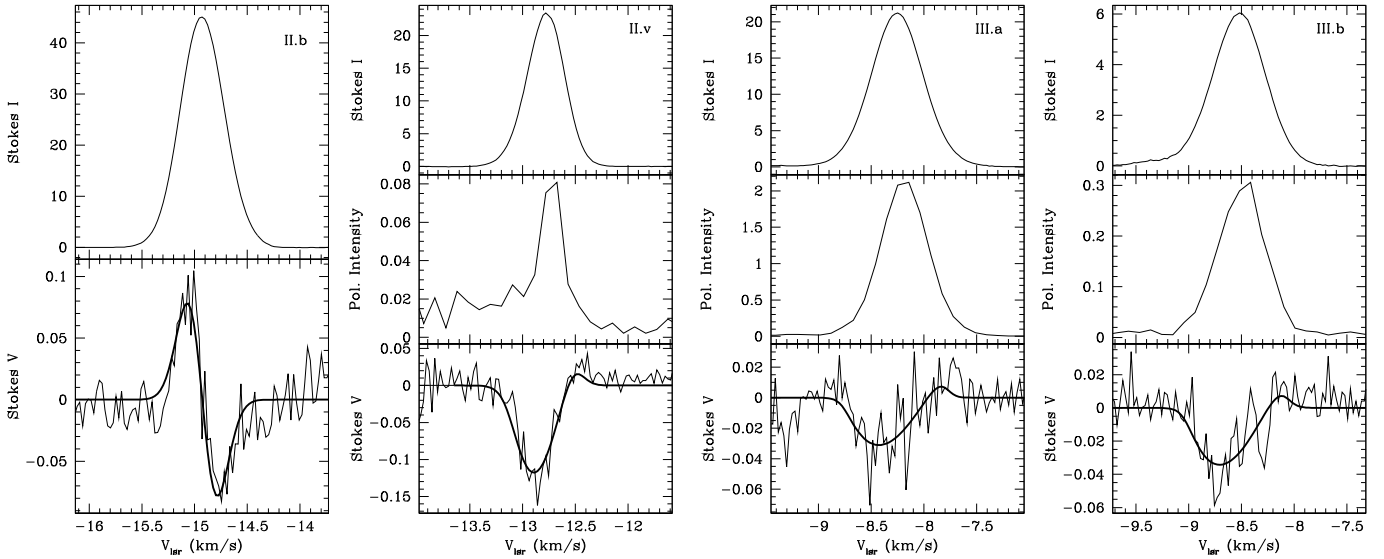

Fig. 5. Similar to Fig. 4 for selected H$_2$O masers in Field II and both features in Field III.

fractional linear polarization P_l is given in Table 1. Figs. 4 and 5 also show several linear polarization spectra. Table 1 lists the weighted mean polarization vector position angle $\langle \chi \rangle$ determined over the maser FWHM for the linearly polarized maser features with corresponding rms error. The weights are determined using the formal errors on χ due to thermal noise, which

are given by $\sigma_\chi = 0.5 \, \sigma_P/P \times 180°/\pi$ (Wardle & Kronberg, 1974). Here P and σ_P are the polarization intensity and corresponding rms error respectively. Fig. 3 shows the linear polarization vectors scaled logarithmically according to fractional polarization.

Table 1. Results

Feature	RA offset (mas)	Dec offset (mas)	Peak Flux Density (I) (Jy beam^{-1})	V_{lsr} (km s^{-1})	Δv_{L} (km s^{-1})	P_l (%)	$\langle\chi\rangle$ (°)	P_V (×10^{-3})	$B_{\parallel}$ [a] (mG)	Δv_{th} [a] (km s^{-1})	$\log(T_b\Delta\Omega)$ [a]
I.a*	44.213	-57.325	10.32	-1.86	0.53	-	-	-	-	-	-
I.b	43.289	-56.585	16.79	-3.83	0.59	0.28 ± 0.12	13 ± 8	2.6	62 ± 12	1.8	10.5
I.c	42.750	-56.510	9.83	-4.12	0.70	0.44 ± 0.06	35 ± 8	9.5	−290 ± 47	2.0	10.7
I.d**	42.290	-47.644	19.09	-4.28	0.58	0.78 ± 0.06	−46 ± 3	12.7	−279 ± 69	-	-
I.e	42.229	-48.655	75.18	-3.96	0.78	0.64 ± 0.04	−47 ± 8	10.3	205 ± 40	1.0	10.0
I.f*	34.428	1.488	33.35	-13.04	0.48	-	-	-	-	-	-
I.g*	33.811	1.977	27.49	-12.97	0.53	-	-	-	-	-	-
I.h*	32.322	-46.771	87.44	-1.94	0.62	-	-	-	-	-	-
I.i*	31.031	-47.121	12.81	-1.68	1.01	-	-	-	-	-	-
I.j*	29.643	-47.557	8.49	-1.20	0.94	-	-	-	-	-	-
I.k	1.963	-1.027	3.48	-18.83	0.57	< 0.86	-	-	< 206	-	-
I.l	1.040	-2.099	3.04	-19.04	0.51	< 0.99	-	23.1	527 ± 109	2.0	9.9
I.m	0.082	-3.303	11.47	-19.44	0.50	< 0.26	-	6.8	135 ± 26	1.7	10.3
I.n	0.000	0.000	78.94	-15.72	0.52	< 0.04	-	7.2	148 ± 34	1.7	10.4
I.o	-0.820	-4.152	4.02	-19.28	0.59	1.17 ± 0.19	8 ± 9	-	< 256	-	-
I.p	-0.871	-0.183	61.63	-15.89	0.51	0.42 ± 0.02	58 ± 2	6.9	−150 ± 42	2.0	9.8
I.q**	-1.486	-1.359	46.82	-16.78	0.68	0.59 ± 0.26	39 ± 2	6.8	−203 ± 71	-	-
II.a	925.674	13.463	18.07	-14.91	0.51	0.33 ± 0.09	−41 ± 5	-	< 22	-	-
II.b	924.445	13.075	44.81	-14.93	0.49	< 0.07	-	3.5	−54 ± 9	1.5	9.8
II.c	906.332	6.070	2.76	-14.25	0.48	< 1.09	-		< 140	-	-
II.d	896.763	3.990	15.24	-14.06	0.51	0.52 ± 0.01	9 ± 7	-	< 34	-	-
II.e	894.765	3.352	21.08	-13.99	0.59	0.37 ± 0.05	−12 ± 10	-	< 28	-	-
II.f	892.838	2.587	24.33	-14.09	0.46	0.21 ± 0.05	38 ± 12	-	< 30	-	-
II.g	890.204	1.947	3.79	-13.99	0.33	< 0.79	-	-	< 88	-	-
II.h	888.068	3.166	3.20	-13.55	0.40	3.44 ± 1.13	−78 ± 4	-	< 125	-	-
II.i	887.387	1.437	33.64	-13.70	0.50	0.15 ± 0.02	−50 ± 16	-	< 15	-	-
II.j	885.188	0.222	8.03	-13.60	0.47	1.05 ± 0.10	6 ± 4	-	< 59	-	-
II.k*	882.617	-0.579	11.25	-13.47	0.53	-	-	-	-	-	-
II.l*	881.495	-0.880	6.95	-13.31	0.47	-	-	-	-	-	-
II.m*	880.610	0.001	5.86	-13.26	0.46	-	-	-	-	-	-
II.n*	876.069	-4.921	5.25	-12.81	0.40	-	-	-	-	-	-
II.o*	875.052	-5.871	5.03	-12.81	0.44	-	-	-	-	-	-
II.p	870.917	-11.180	2.48	-12.57	0.47	< 1.21	-	-	< 190	-	-
II.q	869.659	-11.433	5.84	-12.65	0.50	< 0.51	-	3.5	66 ± 33	1.8	10.2
II.r*	858.940	-15.758	7.85	-12.91	0.41	-	-	-	-	-	-
II.s*	857.685	-16.246	8.92	-12.91	0.40	-	-	-	-	-	-
II.t	855.098	-11.502	5.21	-14.51	0.55	0.41 ± 0.07	86 ± 19	-	< 127	-	-
II.u*	854.380	-17.668	56.09	-12.83	0.42	-	-	-	-	-	-
II.v	853.907	-18.350	23.43	-12.78	0.41	0.34 ± 0.09	84 ± 7	5.7	69 ± 11	1.1	9.7
III.a	143.668	-530.929	21.04	-8.25	0.58	10.8 ± 0.9	66 ± 1	1.8	33 ± 10	1.2	10.7
III.b	142.096	-532.309	6.02	-8.52	0.57	5.0 ± 0.8	62 ± 2	6.9	128 ± 36	1.3	10.5
IV.a	60.131	229.423	1.49	-21.28	0.62	< 2.01	-	-	< 520	-	-
IV.b	60.025	226.307	2.28	-21.07	0.65	1.35 ± 0.24	64 ± 2	-	< 356	-	-
IV.c	58.833	240.075	1.38	-20.75	0.86	< 2.17	-	-	< 779	-	-

[a] Best fit results for the magnetic field strength $B_{\parallel}$ along the line of sight (mG), intrinsic maser thermal width Δv_{th} (km s^{-1}) and emerging brightness temperature $T_b\Delta\Omega$ (K sr) derived as described in Appendix A

* suffer from interference (see text)

** no direct fit possible (see Appendix A)

The strongest linear polarization (~11%) was detected on the brightest maser feature in Field III, but on average P_l ~0.5%. In Fig. 6 we show a channel map of the 2 maser features detected in Field III including their polarization vectors. We do not find any relation between maser brightness and fractional linear polarization.

4. Discussion

Before discussing the polarization results we first determine several intrinsic properties of the masers that are needed for the further analysis of the linear and circular polarization. We also discuss the maser morphology in the 4 fields.
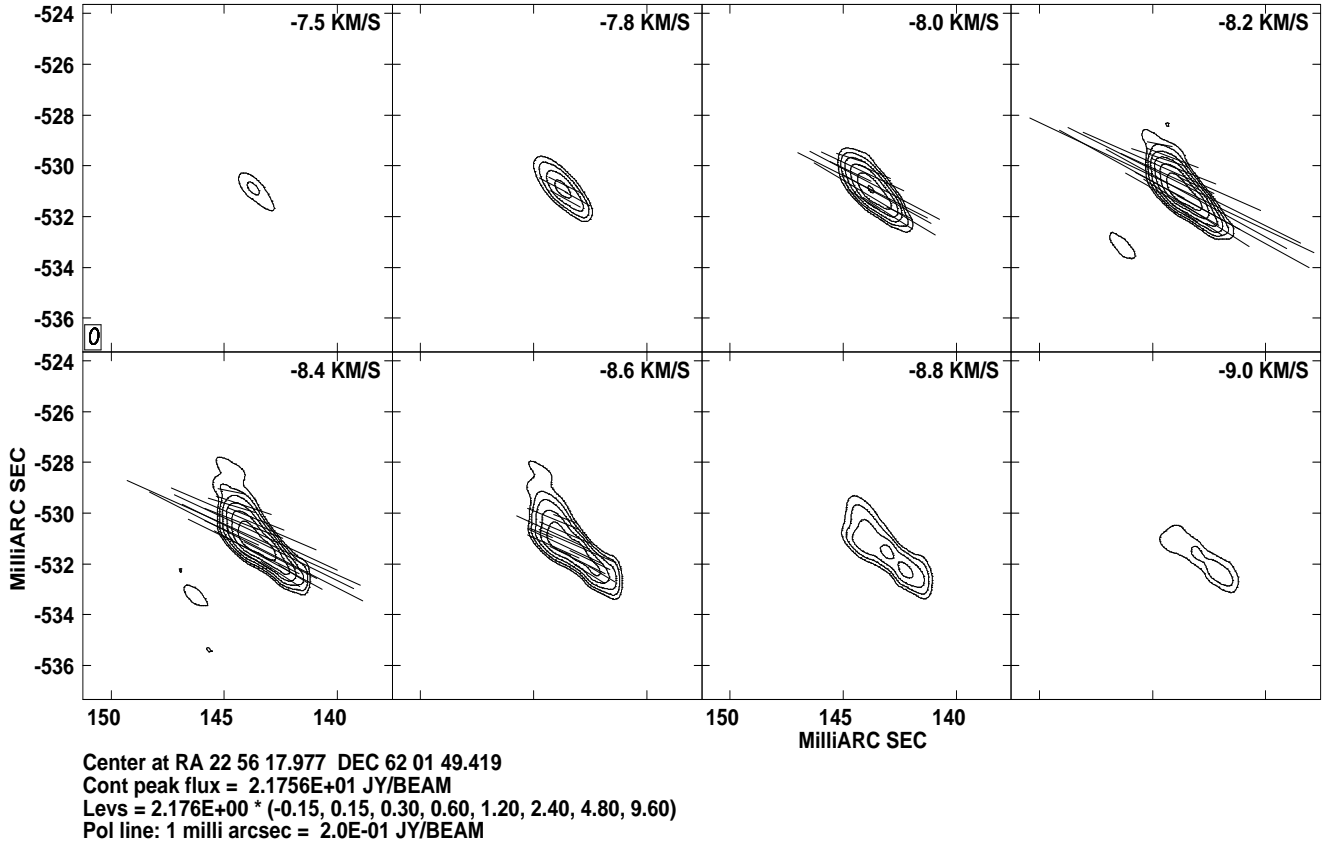
Fig. 6. Channel maps of linear polarization of the elongated H_2O maser feature of Field III which has the highest linear polarization fraction. The bars show the strength and orientation of the polarization vectors.

4.1. Intrinsic Thermal Width, Brightness Temperatures and Maser Beaming

As the model results give the intrinsic thermal width Δv_{th} in the maser region, we can use it to estimate the temperature. Although the error on Δv_{th} is relatively large due to velocity gradients along the maser (Vlemmings & van Langevelde, 2005), we find that on average, Δv_{th}, and correspondingly the temperature, is greater in Field I than in the outlying fields II and III. While in Field I $T \sim 1150$ K, in Field II and III the corresponding temperature is closer to 750 K. These temperatures are an indication that the masers originate in a C-type (non-dissociative) shock instead of a J-type (dissociative) shock. In the latter, the H_2O masers have been found to originate in a relatively narrow range of temperatures near 400 K (with 500 K as a conservative upper bound) at which hydrogen molecules recombine. In contrast, in C-type shocks, the H_2O masers can occur in gas with temperatures up to ~ 3000 K provided the shock velocity $v_s > 10$ km s^{-1} (Kaufman & Neufeld, 1996). The C-shock origin of the masers in Field I is in agreement with the model in G03 where the masers originate in a C-shock expanding though a circumstellar disk.

In addition to Δv_{th} the models also provide an estimate of the emerging brightness temperature $T_b \Delta\Omega$. This can be compared with the values determined from the measurements of the maser flux density and feature sizes. We find that in Field I the majority of the maser features are unresolved. Taking 0.4 mas as the typical size of a H_2O maser feature, we derive a the brightness temperature of $T_b \approx 1.4 \times 10^{11}$ K for a feature of 10 Jy beam^{-1}. Thus, our strongest maser feature in Field I has $T_b \approx 1.1 \times 10^{12}$ K. In the other fields, several of the masers are marginally resolved, with typical feature sizes of ~ 0.6 mas, corresponding to $\sim 7.5 \times 10^{12}$ cm. This implies, for the strongest 54 Jy beam^{-1} maser feature in those regions, $T_b \approx 3.4 \times 10^{11}$ K. Comparing these values with the emerging brightness temperatures $T_b \Delta\Omega$ from our models yields an estimate for the beaming solid angle $\Delta\Omega$. In Field I, with an average $\langle T_b \Delta\Omega \rangle \approx 1.8 \times 10^{10}$ we find, for the maser features with circular polarization, $\Delta\Omega \approx 7 \times 10^{-3}$–$3 \times 10^{-1}$ sr. However, as the features are unresolved the beaming angle may be overestimated. The masers in Field II show a similar range of beaming angle, with $\Delta\Omega \approx 2 \times 10^{-2}$–$4 \times 10^{-1}$ sr while the beaming of the maser in Field III is much less pronounced, as $\Delta\Omega \approx 0.5$. In a tubular geometry the maser beaming $\Delta\Omega \approx (d/l)^2$, where d and l are the transverse size and length of the tube respectively, this implies that, assuming d is approximately the size of the maser features, the maser lengths are ~ 1–6×10^{13} cm. In Field III, the beaming angle is similar to what is expected for a spherical maser that is approaching saturation (Elitzur, 1994).
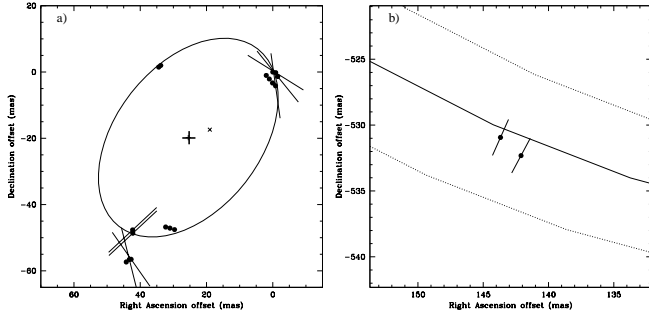
Fig. 7. a) The masers of Field I with the disk-model of G03. We fitted a Right Ascension and Declination offset of the disk center (denoted by the plus sign) as well as a Radius (R_d = 34 ± 4 mas). The inclination angle of 50° and P.A. of 142° were taken from G03. The diagonal cross is the disk center position determined by G03 which has an error of ≈27 mas in each coordinate. The vectors on the maser features are the polarization vectors, which for most of the features is expected to be parallel to the magnetic field direction (see § 4.3). b) The masers of Field III with the expanding shell model of T01a. The solid line is the shell using the updated proper motion and expansion velocity parameters of G03. The dashed lines are the 3σ confidence interval. The vector on the maser features indicate the magnetic field direction (see § 4.3).

We now compare our measured and derived maser brightness temperatures with the maser brightness temperature T_S at the onset of saturation when the ratio between maser rate of stimulated emission (R_m) and the maser decay rate (Γ), $R_m/\Gamma \approx 1$. Using the expression from Reid & Moran (1988):

$$T_S \Delta\Omega = h\nu\Gamma 4\pi/2k_B A, \qquad (1)$$

where h is the Planck constant and k_B the Boltzmann constant, ν is the maser frequency and $A = 2 \times 10^{-9}$ s^{-1} is the 22 GHz H_2O maser spontaneous emission rate (Goldreich & Keeley, 1972). For $\Gamma = 1$ s^{-1} we thus find $T_S \Delta\Omega = 3.4 \times 10^9$ K sr. Nearly full saturation is reached when $R_m/\Gamma \approx 100$, for $T_b \Delta\Omega \approx 3.4 \times 10^{11}$ K sr. This indicates that in Field II the masers are likely mostly unsaturated, while those in Field I are in the onset of the saturation regime. In Field III the masers are almost fully saturated, which is consistent with their strong linear polarization (see Appendix A below). When saturated, the maser radiative transfer equation can be approximated by $T_B/T_S \approx g_0 l$ where g_0 is the maser gain at line center for the unsaturated regime. For the masers in Field III we then find $g_0 l \approx 8$, indicating that for $l \approx 1.5 \times 10^{13}$ cm estimated from the beaming angle, $g_0 \approx 5 \times 10^{-13}$ cm^{-1}.

4.2. H_2O Maser Morphology

As can be seen in Figs. 2 and 3 the H_2O masers around Cepheus A HW2 show a large variety of structures. In our observations several of the maser structures found in T01b and G03 were not detected, even though our sensitivity is within a factor of 2 of those of T01b (∼6 mJy) and G03 (∼25 mJy).
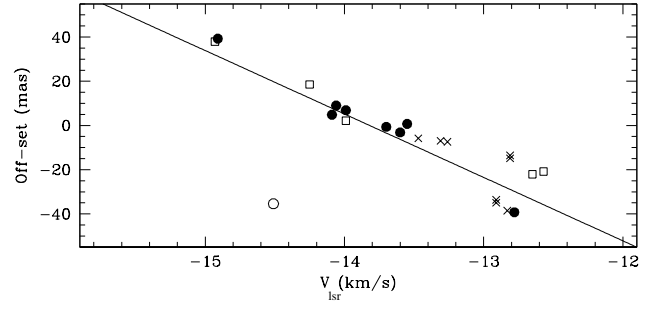
Fig. 8. The velocity of the H_2O maser features making up the filament detected in Field II vs. angular off-set from the center of the filament. The solid and open circles are the maser features that have detected linear polarization while the open squares are the features for which we determined upper limits to P_l. The crosses are the features that are affected by the interference described in §.2 and which were excluded from our polarization analysis. The open circle is a feature that likely does not belong to the filament and which has been excluded in the subsequent analysis. The solid line is a best fit relation between the maser velocity and position off-set.

We did detected a strong linear maser structure in Field II that was not observed in the previous observations. The changes in observed morphology are likely due to the rapid variability of the H_2O masers of Cepheus A, which show variations on timescales as short as a few days (Rowland & Cohen, 1986). Here we discuss the masers of the 4 distinct regions detected in our observations.

Field I: The H_2O masers in this field show the most complex structure. The masers are located ≈150 AU on the sky south of the continuum source HW2 and have been previously detected in T96, T01b and G03. In T01b this region was named R4 and it was proposed that the masers of the NW corner (named R4-A) originate in a bow-shock structure produced by the wind of an undetected protostar near R4-A. The features in the SE could be connected to R4-A and produced by a shock moving ∼4–7 km s^{-1} to the NE. In G03, where these masers were observed with MERLIN, the masers are, instead of in a bowshock, hypothesized to occur in an expanding shockwave in a rotating proto-stellar disk enclosing a central mass of ∼3 $M_\odot$. Here we only detect several bright features making up an incomplete disk with $V_{lsr} \approx -4.0, -1.5$ and -19.0 km s^{-1}. We fitted our maser feature positions to the disk proposed by G03 using a flux density weighted least square method. Keeping the inclination and position angle fixed with the G03 model values (50° and 142° respectively) a fit was made for the Right Ascension and Declination offset of the disk center and for the disk Radius (R_d). The result is shown in Fig. 7a. Our disk center offset position is only ∼7 mas SW of the position determined by G03 while the error on the reference position determination in this paper combined with that of G03 is estimated to be ∼27 mas. Our fitted disk radius $R_d = 34$ mas. Considering we only detect a small part of the disk and since the masers in the SE corner are spread over a large area we es-

timate the systematic error in our radius determination to be 4 mas, larger than the formal fitting uncertainty of ~1 mas. Comparing R_d with the radius determined at Epoch 2000.27 by G03 ($R_d = 38.1 \pm 0.1$ mas) we find that the disk has not expanded in the 4 years after their observations. It possibly even decreased in radius. In G03 it was found that the expansion velocity decreased from 30–40 km s^{-1} in 1996 to ~13 km s^{-1} in 2000. This strong deceleration apparently has continued and may be due to mass loading of the disk as matter is swept up during the expanding shockwave. As a result a stationary shock may have formed where the circumstellar outflow collides with the much denser surrounding medium. This could also explain the disappearance of the brightest disk masers observed in G03, since for higher shock number densities ($\gtrsim 10^{12}$ cm^{-3}) the masers will be quenched.

Field II: The H$_2$O masers in Field II make up a newly discovered filamentary structure ~690 AU East of HW2 at a position angle (PA) of $66.0° \pm 0.2°$ and with a length of ~60 AU. This structure also nearly coincides with 12 GHz methanol masers (at different V_{lsr}) located ~40±10 mas to the NW, which show a linear structure with similar PA. As seen in Fig. 8 there is a velocity gradient along the filament from ~-15 km s^{-1} in the NE to ~-12.5 km s^{-1} in the SW. The maser structure bears resemblance to the masers in R1, R2 and R3 of T01 found towards the West of HW2 with a similar PA, although the masers in Field II are all blue-shifted with respect to the systematic velocity of HW2 while those in R1, R2 and R3 were red-shifted. The masers are too far East to be considered part of the rotating maser disk around HW2 which is thought to have a radius of 300 AU (T96). The elongated appearance of the Field II maser structure suggests a shocked nature as expected from maser theory (Elitzur et al., 1989). Although it is located at a significant distance from HW2 we suggest that the maser structure is due to the interaction of the HW2 outflow with the circumstellar molecular cloud medium. Then, similarly as for the Western R1 features in T01b, the velocity shift of ~2.5 km s^{-1} along the maser filament could be due to acceleration of maser gas by the YSO outflow. If the masers are indeed created by shocks induced by the HW2 outflow this would indicate that at ~690 AU the outflow has an opening angle of ~115°, similar to the opening angle of ~110° estimated for the R1 masers at 150 AU in T01.

Field III: The 2 maser features detected in Field III, approximately 550 AU South of HW2 at $V_{\mathrm{lsr}} \approx -8.5$km s^{-1}, likely belong to the arc structure R5 described in T01a and T01b. These masers are thought to be part of a spherical shell surrounding a protostar that has possibly been identified in Curiel et al. (2002). We do not detect the long maser arc seen in T01a and T01b. While the brightest maser feature in our observations of Field III is $\simeq 20$ Jy beam^{-1}, the brightest maser features of R5 in T01a and T01b (separated by 8.5 yr with respect to our observations) had flux densities of $\simeq 200$ Jy beam^{-1}. However, the PA (~41°) of the extended maser structure of our observations (seen in Fig. 6) agrees with the direction of the maser curve. Fig. 7b shows the maser shell from T01a extrapolated in time using the updated shell parameters determined in G03. The curves indicate a shell expansion of 2.5 ± 0.1 mas yr^{-1} and a motion of the expansion center of 1.4 ± 0.1 mas yr^{-1}

toward PA 126°. The near-perfect alignment of the expanding shell with the maser features is remarkable, as we earlier estimated our reference position to be accurate to ~25 mas. This likely indicates that we underestimated our positional accuracy and that the actual accuracy is better than ~10 mas. In addition, our results indicate that the maser shell has been freely expanding during the past 8.5 years without any indication of deceleration.

Field IV: The masers in Field IV are weak and are aligned at a PA ~ $-6°$. They are located within ~75 AU of HW2 at $V_{\mathrm{lsr}} \approx -21.0$km s^{-1} and are probably part of the rotating maser disk around HW2 proposed in T96.

4.3. Linear Polarization

Linear polarization is often affected by Faraday Rotation due to free electrons along the line of sight through the interstellar medium. However, the Faraday rotation induced in a typical molecular cloud with fairly strong magnetic field (size D ~0.1 pc, electron density n_e ~1 cm^{-3} and $B_{\parallel}$ ~1 mG) is only ~ 0.9° at 22.235 GHz. The rotation induced in the extreme condition of a highly magnetized maser cloud (up to 1 G) is similar or less. As no compact HII regions, in which Faraday rotation could be significant, are located in front of the maser features, we can safely assume the measured χ is not affected by Faraday rotation.

As discussed in Appendix A, the polarization vectors determined from polarization observations of masers in a magnetic field are either parallel or perpendicular to the magnetic field lines. Thus, the polarization vectors contain information on the morphology of the magnetic field but suffer from a 90° degeneracy. The fractional linear polarization depends on the maser saturation level as well as the magnetic field angle θ. Thus, we can use the measurements of P_l together with our model results for the saturation level (through the emerging brightness temperatures) to lift the degeneracy between the polarization vectors and the direction of the magnetic field for several of our maser features.

The polarization vectors observed in the maser fields around Cepheus A HW2 are shown in Fig. 3 while P_l is listed in Table 1. The strongest linear polarization $P_l \approx 11\%$ was found in Field III. This is consistent with the fact that the brightness temperature analysis concluded that the masers in this field are saturated. Using the brightness temperature determined from the models, adjusted for the difference in maser decay and cross-relaxation rate as described in Appendix A, we find using Fig. A.1, that for the masers in Field III, $65° < \theta < 70°$. As was shown in Vlemmings (2005, hereafter V05) this is the magnetic field angle in the unsaturated (or least saturated) maser core. Thus, as $\theta > \theta_{\mathrm{crit}}$, the magnetic field direction is perpendicular to the polarization vectors. As can be seen in Fig. 7b this means the magnetic field, at PA~155°, is perpendicular to the expanding shell found in T01a and thus radial from the central embedded proto-star.

In Field IV fairly strong linear polarization was detected in one of the weak maser features. As the brightness temperature of these masers is relatively low and they are unlikely to be
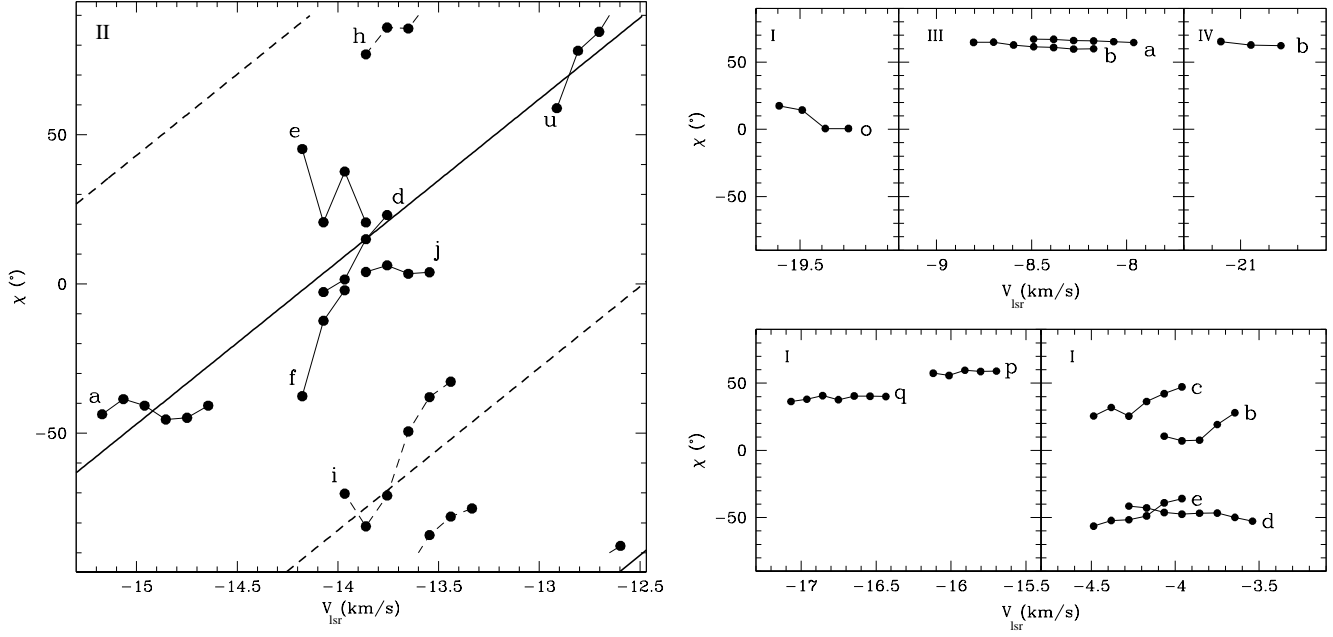
Fig. 9. (Left) χ for the H_2O maser filament features in Field II that have measured linear polarization vs. their velocity. The connected dots belong to the individual features which are labeled with the feature identifier. We excluded the seemingly unrelated feature denoted by the open circle in Fig.8. The thick solid lines (with a 180° ambiguity) is a linear fit to the change in χ along the feature. The thick dashed lines indicates the linear fit when including the 90° flip in χ with respect to the magnetic field direction when the magnetic field angle to the line-of-sight θ becomes larger than θ_{crit} ~55°. For the features connected with the solid lines we expect the χ to be parallel to the direction of the magnetic field while for those connected with dashed lines, χ is perpendicular to the magnetic field. (Right) χ for the H_2O maser in Field I, III and IV that have measured linear polarization vs. their velocity. The connected dots belong to the individual features that are labeled with their corresponding identifier. The boxes are labeled with the field number.

saturated, $P_l = 1.35\%$ indicates that the magnetic field angle $\theta > 70°$. Thus also in Field IV the magnetic field direction is perpendicular to the polarization vector with a PA~154°, more or less along the large scale maser disk proposed in T96 with a PA~135° and radial toward HW2.

The H_2O masers in the circumstellar disk of Field I are found to have $P_l < 1\%$, consistent with their being only slightly saturated. With T_b determined earlier, we find, again using Fig. A.1, that θ is either close to θ_{crit} or $\theta < 25°$. As seen in Fig. 7a, the polarization vectors mostly lie along the disk curvature for most features except I.c and I.d, where we could be seeing a 90° flip. If we assume that for all features, except I.c and I.d, $\theta \lesssim \theta_{crit}$, the magnetic field in Field I lies along the disk. However, if most features have $\theta \gtrsim \theta_{crit}$ except for I.c and I.d, the magnetic field is radial in the H_2O maser region of the rotating disk. Additionally, as in either case, θ is close to $\theta_{crit} = 55°$ the magnetic field angle with respect to the line-of-sight is similar to the disk inclination axis, which would imply the magnetic field lies in the plane of the disk. However, as seen in Table 1, the magnetic field direction changes between the neighboring maser features making a large scale alignment unlikely.

Now we show that the polarization characteristics of the masers in Field II are consistent with the interaction between a

radial magnetic field in the outflow of HW2 and a magnetic field perpendicular to the Galactic plane in the surrounding molecular cloud. The fractional polarization of the maser in the filamentary structure of Field II is on average slightly less than that in Field I. This is expected since the masers in Field II were found to be unsaturated. The high polarization of feature II.h likely indicates that there θ is close to 90°. As seen in Fig. 3, there is evidence of a gradient in polarization angles along the maser filament. In addition to the gradient along the maser filament, we see in the left panel of Fig. 9 that the polarization angle χ rotates across individual maser features, similar to that seen in the cocoon masers of Leppänen et al. (1998). Such rotation of χ is not observed for any of the maser features of the other fields shown in the right panels of Fig. 9. The variation of χ with velocity can be described with a linear gradient, using an flux density weighted least square method allowing for the 90° flip in χ that occurs when $\theta > \theta_{crit}$. We find that χ increases linearly from ~ −50° on the maser feature in the NE to ~90° on the feature in the SW. This implies that II.h and II.i undergo the 90° flip which was already expected for II.h due to its high polarization.

Similar to the model for the variation in polarization angle χ, we have constructed a model for the variation of the angle between the magnetic field direction and maser propagation

axis θ along the maser filament. The model, shown in Fig. 10, is fully consistent with the maser brightness temperatures and the fractional linear polarizations as well as the inferred 90° flip of polarization angle. We have determined θ and its error bars from the relation between P_l and θ for unsaturated masers shown in Fig. A.1. (Note that to the accomodate the direction change of the magnetic field, the model θ ranges from 0° to 180°, with the direction change occurring at $\theta = 90$°). We find that the polarization measurements are consistent with an initial slow change in θ until halfway along the filament the magnetic field changes sign over ≈ 10 mas.

Combining the χ and θ variation models we thus find that at the NE corner of the filament the magnetic field is pointing toward us with $\theta \sim 10$° and PA~ -50°, while in the SW corner it is pointing away from us with $\theta \sim 20$° and PA~ 90°. We interpret this change of the magnetic field as being due to the interaction of the magnetic field related to the HW2 YSO outflow and that related to the surrounding medium. Although the magnetic field structure in the Cepheus A region is complex, Jones et al. (2004) find using Near Infrared imaging polarimetry, that the large scale field threading Cepheus A is almost perpendicular to the galactic plane with PA= 125°. This corresponds to PA=−55°, consistent with $\chi = -50$° found in the NE corner of the maser filament. Jones et al. (2004) also argue that the magnetic field in the HW2 outflow is radial with respect to HW2. This implies an angle of 115° at the location of Field II, very consistent with the PA in the SW corner of the H$_2$O maser filament, especially as we are probably not probing the full polarization vector rotation along the filament.

4.4. The Magnetic Field

4.4.1. The Magnetic Field Strength

The magnetic field strength was determined from circular polarization measurements for 14 maser features in Field I, II and III. In Field I the magnetic field strength varies from $B = -290$ to 527 mG, while in the other fields we find B between -54 and 128 mG. While these latter magnetic field strengths are comparable to the typical field strength determined from other H$_2$O maser observations (10–100 mG), the field strengths determined in Field I are several times higher. However, previous observations were typically performed using single-dish (e.g. Fiebig & Güsten, 1989) or lower resolution interferometers (e.g Sarma et al., 2002), and due to blending of a large number of maser features, the magnetic field strength determined with single-dish and VLA observations could be more than a factor of 2 smaller than the actual field strengths (Sarma et al., 2001). The only other H$_2$O maser magnetic field strength for Cepheus A was determined by Sarma et al. (2002) with the VLA, who found B =-3.2 mG for a feature located more than 2 arcsec East of our observed maser region.

An additional complication to the accurate determination of magnetic field strengths is the occurrence of velocity gradients along the maser amplification path. This was investigated in V05, where it was found that for velocity gradients of ~ 1.5 km s^{-1} along the maser, the magnetic field could be underestimated by ~ 40%. From a total intensity line profile
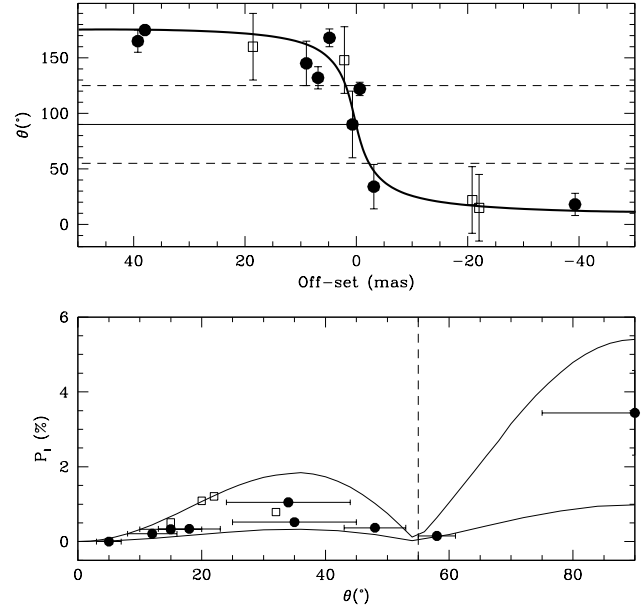

Fig. 10. (bottom) The magnetic field angle θ estimated from the fractional polarization P_l measurement. The vertical dashed line indicates θ_{crit}. The solid dots are the measured P_l of the Field II maser features and the open squares are upper limits. The error bars in θ are determined from the allowed range of θ in the P_l vs. θ models of V05 shown for masers with emerging brightness temperatures $T_b\Delta\Omega = 10^9$ and 10^{10}K sr. (lower and upper solid line respectively). (top) A model for the change of magnetic field angle θ along the H$_2$O maser filament. The thick solid line is the proposed model. The solid horizontal line indicates where the magnetic field direction changes. Between the dashed horizontal lines, which denote θ_{crit}, the polarization vectors are perpendicular to the direction of the magnetic field. Above and below θ_{crit} the polarization vectors are parallel to the magnetic field.

analysis as described in Vlemmings & van Langevelde (2005) we estimate the typical velocity gradient for our masers to be ~ 1 km s^{-1}. For partly or fully saturated masers with $\Delta v_{\mathrm{th}} > 1.5$ km s^{-1}, V05 finds that the magnetic field is overestimated by not more than a few percent. However, for the unsaturated masers in Field II the field strengths have most likely been underestimated by ~ 30%.

The magnetic field dependence on θ introduces further uncertainties. While for low brightness temperature masers B is straightforwardly dependent on $\cos\theta$, this relation breaks down for higher brightness temperatures. This was first investigated in Nedoluha & Watson (1992) and later shown in more detail in Watson & Wyld (2001) for masing involving low angular momentum transitions. The specific case for the 22 GHz H$_2$O masers was again shown in V02 and their figure 7 is reproduced here as Fig. A.2. In the figure we see that for increasing saturation there is a large range of θ where the magnetic field is actually overestimated. As we have been able to estimate θ for several of the observed masers we can also estimate

the influence on the magnetic field strength. For the masers in Field I θ is thought to be close to θ_{crit}, while the masers are saturating. This means the actual magnetic field is approximately 10% higher than the measured field strength. Thus we estimate the average field in Field I to be ~250 mG with a maximum of ~650 mG. The masers in Field II are however mostly unsaturated and as a result $|B| = B_{\parallel}/\cos\theta$. As we only detected a magnetic field strength at the edges of the filament, where we estimated θ to be between 10° and 20°, the field in the NE of the filament is ~55 mG pointing toward us while it is ~70 mG and pointing away from us in the SW. Finally, the masers in Field III were found to have $65° < \theta < 70°$. As they are saturated the magnetic field strength is likely ~20% less than determined from our fits, indicating that $|B| = 30$–100 mG.

Aside from the large magnetic field strength, the maser structure in Field I is also characterized by field reversals on small scales. The magnetic field is found to reverse over less than 0.1 mas, which corresponds to $\sim 10^{12}$ cm. This argues against a large scale alignment of the magnetic field with the maser disk. The magnetic field is likely frozen into high density maser clumps in a turbulent medium. If the masers exist in a shocked region where the magnetic pressure supports the cloud and dominates the gas pressure higher magnetic fields can be obtained. Using formula 4.5 from Kaufman & Neufeld (1996),

$$B \sim 80\left(\frac{n_0}{10^8\ \mathrm{cm}^{-3}}\right)^{1/2}\left(\frac{v_s}{10\ \mathrm{km\ s}^{-1}}\right)\ \mathrm{mG}, \tag{2}$$

where n_0 is the pre-shock H_2 density and v_s is the shock velocity, we find that for a shock velocity $v_s = 10$ km s^{-1} as estimated for Field I, a magnetic field $B = 600$ mG can be reached if the pre-shock number density $n_0 = 5.6 \times 10^9$ cm^{-1}. Estimating the pre-shock magnetic field using the empirical relation of Crutcher (1999) $B \propto n^{0.47}$ from the density and magnetic field found at the edge of NH_3 molecular clouds ($B = 0.3$ mG, $n = 2 \times 10^4$ cm^{-3}; Garay et al., 1996) yields $B_0 \approx 100$ mG, which is almost 2 orders of magnitude larger than the typical pre-shock magnetic field strength ($\sim$1 mG). Also, when determining the number density of hydrogen in the shocked H_2O maser region using the relation from Crutcher (1999), the magnetic fields imply densities $n_{H_2} = 5 \times 10^9$–2×10^{11} cm^{-3}. While the low-end values for n are reasonable for H_2O masers, the high end ($> 10^{10}$ cm^{-3}) is unlikely, as such high densities quench the maser population inversion. Thus, the magnetic field strength in the pre-shock medium of the proto-stellar disk is likely enhanced by the pressence of a nearby magnetic dynamo.

Using Eq. 2 to estimate the pre-shock number density near the maser filament in Field II yields, assuming $v_S = 13$ km s^{-1} similar to the shock velocity in R1 to R3 of T01b, $n_0 = 3 \times 10^7$–1×10^8 cm^{-3}. Scaling with $B \propto n^{0.47}$ this implies, for the pre-shock magnetic field $B_0 \approx 10$–15 mG, similar to the magnetic field determined for comparable densities in the OH masers of Cepheus A (Bartkiewicz et al., 2005). For the number density in the shocked region this implies $n_{H_2} = 3.5 \times 10^8$–$4.7 \times 10^9$ cm^{-3}, typical for H_2O masers.

4.4.2. The influence of the Magnetic Field

We now examine the influence of the magnetic field on the molecular outflow around HW2. When the magnetic field pressure becomes equal to the dynamic pressure in the outflow the magnetic field will be able to influence or even control the molecular outflow. Defining B_{crit} the critical magnetic field where the dynamic and magnetic pressure are equal, we find

$$B_{\mathrm{crit}} = (8\pi\rho v^2)^{1/2}, \tag{3}$$

where ρ and v are the density and velocity of the maser medium respectively. Assuming an outflow velocity of ~13 km s^{-1} we find $B_{\mathrm{crit}} \approx 30$, 100 and 350 mG for number densities of $n_{H_2} = 10^8$, 10^9 and 10^{10} cm^{-3} respectively. This means that in all the H_2O maser regions where we measured the magnetic field strength the magnetic pressure is approximately equal to the dynamic pressure, as was previously found in Sarma et al. (2002). As OH maser polarization observations indicate that this also holds in the lower density pre-shock regions, we conclude that the magnetic field strength is capable of controlling the outflow dynamics.

5. Summary

Using polarimetric VLBA observations of the H_2O masers around Cepheus A HW2 we have been able to measure the magnetic field strength and direction in great detail at sub-AU scales. We detected H_2O masers over an area of ~1 ″ in 4 distinct fields. For each of the fields we derived physical properties and several intrinsic properties of the masers.

Field I: The H_2O masers in this field occur in what was proposed in G03 to be a spherical shockwave expanding through a circumstellar disk. We find that between the G03 MERLIN observations in 2000 and our observations the maser ring has not expanded and conclude that the expanding shockwave has been severely decelerated, possibly due to mass-loading. From our maser models and the measured brightness temperatures we find that the typical maser beaming angle in this field is ~5×10^{-2} sr implying maser amplification lengths of several AU. The masers are approaching saturation. The magnetic field strength is strong (on average 250 mG and as high as 650 mG) and shows direction reversal on scales of ~10^{12} cm. This can be due to the fact that the magnetic field is frozen into a dense and turbulent medium although the linear polarization vectors indicating the magnetic field direction follow the disk and the magnetic field angle with respect to the line-of-sight θ is approximately equal to the disk inclination. The high magnetic field strengths indicate that the field is enhanced by a nearby magnetic dynamo.

Field II: This field consists of a newly discovered maser filament at ~690 AU East of Cepheus A HW2 with a PA= 66°. It is likely the result of the shock interaction between the HW2 outflow and the surrouding molecular cloud and implies a large opening angle (115°) of the outflow. The maser beaming angle in Field II is ~10^{-2} sr with maser path lengths of ~2 AU while the masers are unsaturated. We find a clear velocity and magnetic field orientation gradient along the filament consistent with the interaction between a radial magnetic field

in the HW2 outflow and the magnetic field in the surrounding Cepheus A complex which is almost perpendicular to the Galactic plane. The magnetic field strength of 50–70 mG is typical for H_2O masers found in SFRs.

Field III: The masers of Field III make up a small part of the shell structure found in T01 and, even though our maser reference position has an estimated error of up to 25 mas, are fully consistent with the shell expansion model parameters estimated in G03. We find a magnetic field strength between 30–100 mG, consistent with other SFR H_2O maser polarization measurements and find that the magnetic field direction is along the shell expansion direction, radial from the central embedded proto-star. As these maser have the highest measured linear polarization, $P_l = 10\%$, we can conclude that they are saturated. The beaming angle is consistent with a spherical maser geometry.

Field IV: Located close to HW2, the maser in this field are weak and no magnetic field strength was determined. The upper limits of $B_\parallel \approx 500$ mG. The linear polarization indicates that the magnetic field is either aligned with the H_2O maser disk around HW2 or radial toward HW2.

6. Conclusions

Strong magnetic fields of up to ~600 mG have been measured in the H_2O masers around Cepheus A HW2. The strongest magnetic fields were measured in the maser structure that was identified as a circumstellar disk (G03), suggesting the nearby presence of a dynamo source. The field strengths determined in the maser regions further from the central source HW2 are 30–100 mG, consistent with earlier VLA, VLBA and single dish measurements of SFRs. The high magnetic field strengths indicate that the magnetic pressure is similar to the dynamic pressure in the outflows around HW2. Thus, the magnetic fields likely play a large role in supporting the molecular cloud and shaping the outflows in this very active high-mass star-forming region.

Appendix A: Polarization Modeling and Analysis

Here we describe the modeling and analysis of the 22 GHz H_2O maser linear and circular polarization used in this paper to determine the magnetic field strength, saturation level and intrinsic thermal line width of the maser features.

A.1. Circular Polarization

For the analysis of the circular polarization spectra we used the full radiative transfer non-LTE interpretation, which was thoroughly described in V02. There the coupled equations of state for the 99 magnetic substates of the three dominant hyperfine components from Nedoluha & Watson (1992) (hereafter
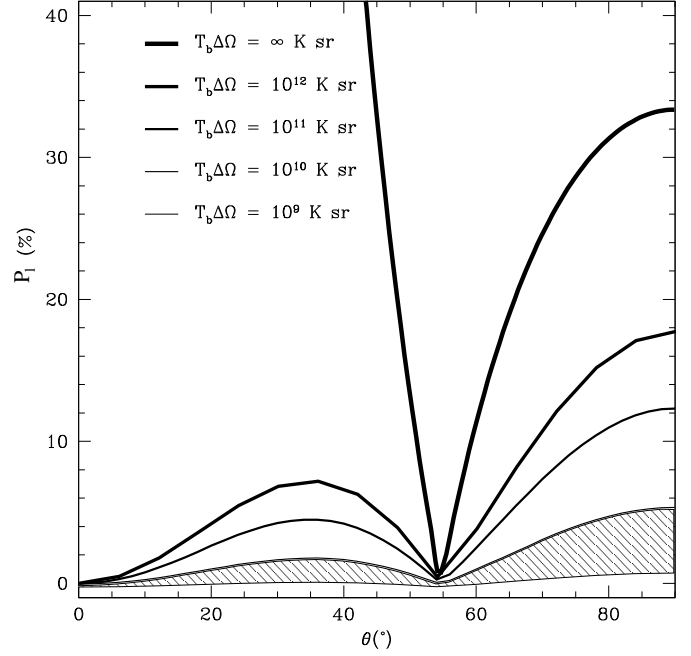

Fig. A.1. The angle θ between the maser propagation direction and the magnetic field vs. the fractional linear polarization P_l for different values of emerging maser brightness (for $[\Gamma+\Gamma_\nu] = 1$ s^{-1}). The thick solid line denotes the theoretical limit from Goldreich et al. (1973) for a fully saturated maser. The shaded area is the region of emerging brightness temperatures found for the masers in Field II.
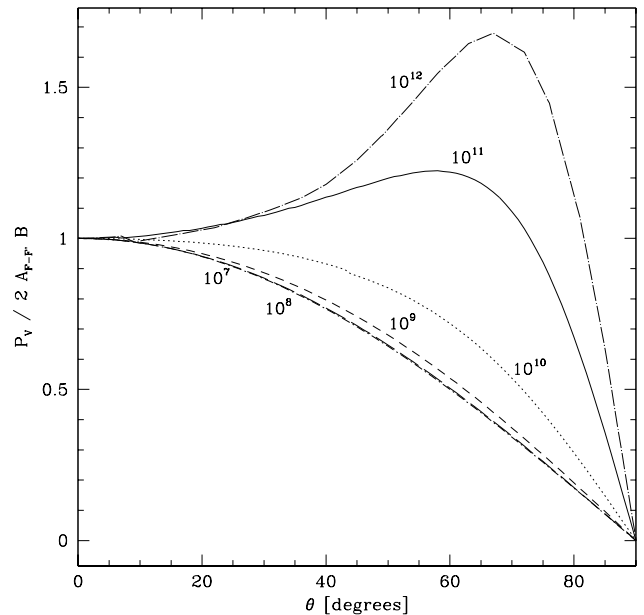

Fig. A.2. θ-dependence of Eq. A.1 for increasing emerging brightness temperature $T_b\Delta\Omega$ (for $[\Gamma + \Gamma_\nu] = 1$ s^{-1}) from V02. The lines for $T_b\Delta\Omega = 10^7$ and 10^8 coincide and are the same as the lines for lower brightness temperatures. For fully unsaturated masers the dependence is equal to $\cos\theta$

NW92) were solved for a linear maser in the presence of a magnetic field. The emerging maser flux densities of the resulting spectra are expressed in $T_b\Delta\Omega$, where T_b is the brightness temperature and $\Delta\Omega$ is the beaming solid angle. It was found in NW92 that the emerging brightness temperature scaled linearly with $(\Gamma + \Gamma_\nu)$, which are the maser decay rate Γ and cross-relaxation rate Γ_ν. For the 22 GHz H_2O masers, Γ is typically assumed to be $\lesssim 1$ s^{-1}. In star-forming regions it has been found that $\Gamma_\nu \approx 2$ s^{-1} for $T \sim 400$ K and $\Gamma_\nu \approx 5$ s^{-1} for $T \sim 1000$ K (Anderson & Watson, 1993) and thus the models from V02 (where $(\Gamma + \Gamma_\nu) = 1$ s^{-1}) have been adjusted to these values.

The model results further depend on the intrinsic thermal line-width Δv_{th} in the maser region, where $\Delta v_{th} \approx 0.5(T/100)^{1/2}$ with T the temperature of the masing gas. Model spectra for a grid of Δv_{th} between 0.8 and 2.5 km s^{-1}, corresponding to temperatures between 250 and 2500 K, were directly fitted to the observed I and V spectra using a least square fitting routine. As described in V02 the spectral fitting for the non-LTE analysis requires the removal of the scaled down total power spectrum from the V-spectrum to correct for small residual gain errors between the right- and left-polarized antenna feeds. This was typically found to be $\sim 0.5\%$ of the total power. The best fit model thus produced the line of sight magnetic field $B_\parallel$ and the thermal line-width Δv_{th} as well as the maser emerging brightness temperature $T_b\Delta\Omega$. However, the uncertainties in Δv_{th} and $T_b\Delta\Omega$ are large, as they are strongly affected by maser velocity gradients (Vlemmings & van Langevelde, 2005; V05). Additionally, $T_b\Delta\Omega$ depends on the actual value of $(\Gamma + \Gamma_\nu)$. We estimate the uncertainties in the fit for Δv_{th} to be ~ 0.3 km s^{-1} and the uncertainty in $\log(T_b\Delta\Omega)$ to be ~ 0.4. As the magnetic field depends on the intrinsic thermal line-width and emerging brightness temperature (V02), this leads to an added uncertainty in the magnetic field determination of $\sim 15\%$ which has been included in the formal fitting errors.

When a direct model fit was not possible, we used the relation between the magnetic field strength B and percentage of circular polarization P_V.

$$P_V = (V_{max} - V_{min})/I_{max}$$
$$= 2 \cdot A_{F-F'} \cdot B_{[Gauss]}\cos\theta/\Delta v_L[\text{km s}^{-1}]. \quad (A.1)$$

Here θ is the angle between the maser propagation direction and the magnetic field ($0° < \theta < 90°$) and Δv_L is the maser full width half maximum (FWHM). V_{max} and V_{min} are the maximum and minimum of the circular polarization and I_{max} is the maximum total intensity maser flux density. The coefficient $A_{F-F'}$ describes the relation between the circular polarization and the magnetic field strength for a transition between a high (F) and low (F') rotational energy level. $A_{F-F'}$ depends on Δv_{th} and maser saturation level as described in NW92 and V02 as well as on velocity and magnetic field gradients along the maser path as shown in V05. We used $A_{F-F'} = 0.012$, which is the typical value we found for the maser of Cepheus A HW2. For maser features where no circular polarization was detected the 3σ upper limits were determined using Eq. A.1 with $P_V = 6\sigma_V/I_{max}$, with σ_V being the rms noise on the maser V-spectrum determined after Hanning smoothing the spectrum ($\sigma_V \sim 5$–8 mJy).

For maser brightness temperatures $T_b\Delta\Omega > 10^9$ K sr it was shown in NW92 that the $\cos\theta$ dependence of Eq. A.1 breaks down introducing a more complex dependence on θ. This was later shown in more detail in Watson & Wyld (2001) for masing involving angular momentum $J = 1$–0 and $J = 2$–1 transitions. In V02, figure 7 shows the derived magnetic field strength dependence on θ to $A_{F-F'}$ for the 22 GHz $J = 6$–5 transition. This figure is repeated here as Fig. A.2.

A.2. Linear Polarization

Maser theory has shown that the percentage of linear polarization P_l of H_2O masers depends on the degree of saturation and the angle θ between the maser propagation direction and the magnetic field (e.g. NW92; Deguchi & Watson, 1990). Figure 7 of NW92 shows the relationship between θ and P_l while their Figure 8 shows the P_l dependence on saturation level. Fig. A.1 shows the dependence of P_l on θ for various emerging brightness temperatures as calculated from the models of NW92 and V02. A high linear polarization fraction ($P_l > 5\%$) can only be produced when the maser is saturated. Additionally, the polarization vectors are either perpendicular or parallel to the magnetic field lines, depending on θ. When $\theta > \theta_{crit} \approx 55°$ the polarization vectors are perpendicular to the magnetic field, and when $\theta < \theta_{crit}$ they are parallel (Goldreich et al., 1973). Consequently, the linear polarization vectors can flip 90° at very small scales as was observed in for instance circumstellar SiO masers (Kemball & Diamond, 1997).

References

Akeson, R. L. & Carlstrom, J. E. 1997, ApJ, 491, 254

Anderson, N. & Watson, W. D. 1993, ApJ, 407, 620

Bartkiewicz, A., Szymczak, M., Cohen, R. J., & Richards, A. M. S. 2005, MNRAS, 361, 623

Bonnell, I. A., Bate, M. R., & Zinnecker, H. 1998, MNRAS, 298, 93

Cohen, R. J., Brebner, G. C., & Potter, M. M. 1990, MNRAS, 246, 3P

Cohen, R. J., Rowland, P. R., & Blair, M. M. 1984, MNRAS, 210, 425

Crutcher, R. M. 1999, ApJ, 520, 706

Curiel, S., Ho, P. T. P., Patel, N. A., et al. 2005, ApJ, submitted

Curiel, S., Trinidad, M. A., Cantó, J., et al. 2002, ApJ, 564, L35

Deguchi, S. & Watson, W. D. 1990, ApJ, 354, 649

Elitzur, M. 1994, ApJ, 422, 751

Elitzur, M., Hollenbach, D. J., & McKee, C. F. 1989, ApJ, 346, 983

Etoka, S. & Diamond, P. 2004, MNRAS, 348, 34

Fiebig, D. & Güsten, R. 1989, A&A, 214, 333

Gallimore, J. F., Cool, R. J., Thornley, M. D., & McMullin, J. 2003, ApJ, 586, 306 (G03)

Garay, G., Ramirez, S., Rodriguez, L. F., Curiel, S., & Torrelles, J. M. 1996, ApJ, 459, 193

Goldreich, P. & Keeley, D. A. 1972, ApJ, 174, 517

Goldreich, P., Keeley, D. A., & Kwan, J. Y. 1973, ApJ, 179, 111

Hughes, V. A. & Wouterloot, J. G. A. 1984, ApJ, 276, 204

Imai, H., Horiuchi, S., Deguchi, S., & Kameya, O. 2003, ApJ, 595, 285

Jiang, Z., Tamura, M., Fukagawa, M., et al 2005, Nature, 437, 112

Johnson, H. L. 1957, ApJ, 126, 121

Jones, T. J., Woodward, C. E., & Kelley, M. S. 2004, AJ, 128, 2448

Kaufman, M. J. & Neufeld, D. A. 1996, ApJ, 456, 250

Kemball, A. J. & Diamond, P. J. 1997, ApJ, 481, L111

Kemball, A. J., Diamond, P. J., & Cotton, W. D. 1995, A&AS, 110, 383

Lada, C. J., Blitz, L., Reid, M. J., & Moran, J. M. 1981, ApJ, 243, 769

Leppänen, K., Liljeström, T., & Diamond, P. 1998, ApJ, 507, 909

McKee, C. F. & Tan, J. C. 2003, ApJ, 585, 850

Minier, V., Conway, J. E., & Booth, R. S. 2001, A&A, 369, 278

Modjaz, M., Moran, J. M., Kondratko, P. T., & Greenhill, L. J. 2005, ApJ, 626, 104

Mouschovias, T. C. & Ciolek, G. E. 1999, in NATO ASIC Proc. 540: The Origins of Stars and Planetary Systems, ed. C. J. Lada & N. D. Kylafis (Dordrecht: Kluwer), 305

Nedoluha, G. E. & Watson, W. D. 1992, ApJ, 384, 185 (NW92)

Patel, N. A., Curiel, S., Sridharan, T. K., et al 2005, Nature, 427, 109

Reid, M. J. & Moran, J. M. 1981, ARA&A, 19, 231

Reid, M. J. & Moran, J. M. 1988, Astronomical masers; in Galactic and Extragalactic Radio Astronomy 2nd ed., ed. G. L. Verschuur & K. I. Kellermann, (Berlin: Springer), 255–294

Rodríguez, L. F., Garay, G., Curiel, S., et al. 1994, ApJ, 430, L65

Rowland, P. R. & Cohen, R. J. 1986, MNRAS, 220, 233

Sarma, A. P., Troland, T. H., Crutcher, R. M., & Roberts, D. A. 2002, ApJ, 580, 928

Sarma, A. P., Troland, T. H., & Romney, J. D. 2001, ApJ, 554, L217

Shu, F. H., Adams, F. C., & Lizano, S. 1987, ARA&A, 25, 23

Torrelles, J. M., Gómez, J. F., Garay, G., et al. 1998, ApJ, 509, 262 (T98)

Torrelles, J. M., Gómez, J. F., Rodríguez, L. F., et al. 1996, ApJ, 457, L107 (T96)

Torrelles, J. M., Patel, N. A., Gómez, J. F., et al. 2001a, ApJ, 560, 853 (T01a)

Torrelles, J. M., Patel, N. A., Gómez, J. F., et al. 2001b, Nature, 411, 277 (T01b)

Vlemmings, W. H. T. 2005, A&A, accepted (V05)

Vlemmings, W. H. T., Diamond, P. J., & van Langevelde, H. J. 2002, A&A, 394, 589 (V02)

Vlemmings, W. H. T. & van Langevelde, H. J. 2005, A&A, 434, 1021

Vlemmings, W. H. T., van Langevelde, H. J., & Diamond, P. J. 2005, A&A, 434, 1029

Wardle, J. F. C. & Kronberg, P. P. 1974, ApJ, 194, 249

Watson, W. D. & Wyld, H. W. 2001, ApJ, 558, L55

This figure "fig3.jpg" is available in "jpg" format from:

http://arXiv.org/ps/astro-ph/0510452v1